HAL open science

Detection of a few DNA copies by real-time electrochemical polymerase chain reaction

M. Moreau, S. Delile, A. Sharma, C. Fave, A. Perrier, B. Limoges, D. Marchal

To cite this version:

M. Moreau, S. Delile, A. Sharma, C. Fave, A. Perrier, et al.. Detection of a few DNA copies by real-time electrochemical polymerase chain reaction. Analyst, 2017, 142 (18), pp.3432-3440. 10.1039/c7an00978j . hal-01929872

HAL Id: hal-01929872

https://hal.sorbonne-universite.fr/hal-01929872v1

Submitted on 8 Jun 2022

HAL is a multi-disciplinary open access archive for the deposit and dissemination of scientific research documents, whether they are published or not. The documents may come from teaching and research institutions in France or abroad, or from public or private research centers.

L'archive ouverte pluridisciplinaire **HAL**, est destinée au dépôt et à la diffusion de documents scientifiques de niveau recherche, publiés ou non, émanant des établissements d'enseignement et de recherche français ou étrangers, des laboratoires publics ou privés.

Distributed under a Creative Commons Attribution - NonCommercial 4.0 International License

Detection of a few DNA copies by real-time electrochemical polymerase chain reaction

M. Moreau,‡[a] S. Delile,‡[a] A. Sharma,[a,b] C. Fave,[a] A. Perrier,*[b,c] B. Limoges *[a] and D. Marchal*[a]

In the current work, accurate quantification over 10 to 10^8 DNA copies has been successfully achieved for the first time by real-time electrochemical PCR. This has been made possible thanks to the combined use of a fully automated house-built electrochemical qPCR device, optimized for parallel heating and electro-chemical monitoring of up to 48 PCR solutions, and the appropriate selection of a DNA intercalating redox probe retaining a strong affinity binding to ds-DNA at the PCR measurement temperature of 72 °C (corresponding to the PCR elongation step). This has also been achieved through the identification of the key parameters governing the onset electrochemical signal decrease and amplitude signal decrease as a function of the PCR cycle for a given DNA intercalating redox probe, thus allowing us to predict the electrochemical PCR kinetic plots from the values of the DNA affinity binding constant determined as a function of temperature. To the best of our knowledge, the analytical performances of the current electrochemical qPCR outperform all of those previously published, in terms of detection limit, dynamic range, reproducibility and melting curve analysis compared to that achieved on a commercialized bench-top fluorescence-based qPCR instrument.

Introduction

Accurately quantifying DNA sequences at the level of a few DNA molecules in complex biological samples using simpler, faster and cheaper nucleic acid detection methods is still an important research goal in molecular diagnostics, food safety or environmental survey.[1] Currently, the most popular and widely used methods are based on *in vitro* DNA amplification techniques such as fluorescence-based quantitative real-time polymerase chain reaction (qPCR).[2] A key advantage of qPCR is that it provides a quantitative approach to determine the concentration of a nucleic acid sequence in a biological sample, leading generally to more accurate and reproducible results than with other molecular biological methods.[2,3] In spite of its effectiveness and frequent use in molecular diagnostics, fluorescence-based qPCR suffers from several drawbacks, namely high cost, poor robustness, and difficulty in integrating the overall optical components in a small-size portable device.[4] These shortcomings preclude the accessibility of qPCR as a very widespread and commonplace bench-top laboratory equipment, as well as a suitable technique for point-of-care genetic testing in limited-resource settings.[5] One possible route to overcome most of the above drawbacks is to substitute the optical fluorescence detection by a simpler, less expensive, more robust, and miniaturizable non-optical readout system. Motivated by these needs, significant progress has been made recently in the development of electrochemical-based real-time PCRs, wherein the amplified targeted DNA is monitored electrochemically *in situ* during the amplification reaction.[6–9] Among the real-time electrochemical detection strategies developed so far, certainly the most promising one in terms of analytical performances and simplicity is the one based on the monitoring of the faradaic current response generated by a ds-DNA intercalating redox probe added to the PCR solution.[8] In this approach, the faradaic signal is exponentially decreased from an onset PCR cycle value that correlates to the initial amount of the targeted DNA. The underlying principle leading to this decrease relies on a reduced rate of mass transport of the free-to-diffuse redox probe as it increasingly intercalates into the amplified ds-DNA.[8] Analytical performances reached with this detection strategy were however not as good as those obtained by fluorescence-based qPCR, reaching a detection limit of $\sim 10^3$ DNA copies per well.[8] This lack of performance

[a]*Laboratoire d'Electrochimie Moléculaire, UMR 7591 CNRS, Université Paris Diderot, Sorbonne Paris Cité, 15 rue Jean-Antoine de Baïf, F-75205 Paris Cedex 13, France. E-mail: marchal@univ-paris-diderot.fr, limoges@univ-paris-diderot.fr*

[b]*Equipe de Chimie Théorique et Modélisation (CTM), Chimie ParisTech, PSL Research University, CNRS, Institut de Recherche de Chimie Paris (IRCP), F-75005 Paris, France. E-mail: aurelie.perrier-pineau@univ-paris-diderot.fr*

[c]*Université Paris Diderot, Sorbonne Paris Cité, 5 rue Thomas Mann, F-75205 Paris Cedex 13, France*

‡These two authors have contributed equally to the work.

has been assumed to result from the use of a non-optimally designed custom-made electrochemical real-time PCR device, leading to the occurrence of a limiting nonspecific amplification response.[8] Another explanation was the absence of a theoretical model to rationally predict and optimize the analytical response as a function of the key parameters governing not only the onset electrochemical signal decrease but also the amplitude signal decrease, both being previously shown to be strongly influenced by the affinity binding constant (K_b) of the intercalating redox probe and the selection of an appropriate redox probe concentration.[8] Here, we propose to investigate in more detail these criteria with the main objective to better understand their relative significance and contribution to the electrochemical qPCR analytical performances. We notably pay special attention to the determination of K_b as a function of temperature for three illustrative intercalating redox probes. Since, during a PCR experiment, the electrochemical measurement is recorded at an elevated temperature (*i.e.*, normally at 72 °C, corresponding to the PCR elongation step), knowing the temperature dependence of K_b is essential for modelling and predicting the electrochemical qPCR response.

Results and discussion

The three redox reporters we have selected are the osmium complex $[Os(bpy)_2dppz]^{2+}$ (E^0 = 0.65 V *vs.* Ag/AgCl), the methylene blue derivative PhP (E^0 = −0.16 V *vs.* Ag/AgCl at pH 8.8), and methylene blue MB (E^0 = −0.28 V *vs.* Ag/AgCl at pH 8.8) (Fig. 1).

At room temperature, these redox probes present significant differences in their intercalating binding strength to ds-DNA, ranging over 2 order of magnitude from ~10^6 M^{-1} for the osmium complex[8,10] to ~10^4 M^{-1} for MB,[11] the K_b of PhP being in between these two values.[12] The probe concentration (C_I^0) was selected so as to have a compromise between the need to avoid a too strong inhibition of PCR at a high concentration and the ability to reliably measure a barely detectable electrochemical response at a low concentration. In the case of probes that do not significantly inhibit PCR, the amplitude signal decrease was also considered with a view to maximize its value. The selected probe concentrations were finally 0.5 μM for the osmium complex and 15 μM for both PhP and MB.

With the aim to compare the three redox probes under similar qPCR conditions, a series of electrochemical qPCR experiments was performed with each probe to amplify the same sample of 10^7 DNA copies of LITMUS 28i vector per electrochemical well. The experiments were achieved with a fully automated house-built electrochemical qPCR device, optimized for parallel heating and electrochemical monitoring of up to 48 PCR solutions (see the ESI† for details).[13] A key advantage of this device is that it allows for a better regulation of the thermal cycles than previously, which is crucial for limiting the non-specific amplifications of primer dimers. The electrochemical detection technique, *i.e.* square wave voltammetry (SWV), was the same as previously.[8] During the PCR reaction, the electrochemical microplate was subjected to 3 step-temperature thermal cycles (denaturation, annealing and elongation) and the content of each electrochemical well was scanned by SWV at the end of each elongation step (*i.e.* at 72 °C). Using a dedicated Matlab program, the SWV faradaic peak charges (Fig. S1, ESI†) were automatically extracted from raw signals after baseline correction and normalisation, and then plotted as a function of PCR cycles to generate the kinetic PCR curves as shown in Fig. 2. The experimental cycle threshold (C_T), defined as the number of cycles required for the electrochemical signal to cross the signal decrease threshold (*i.e.*, exceeding a signal decrease of 3 to 5 times the

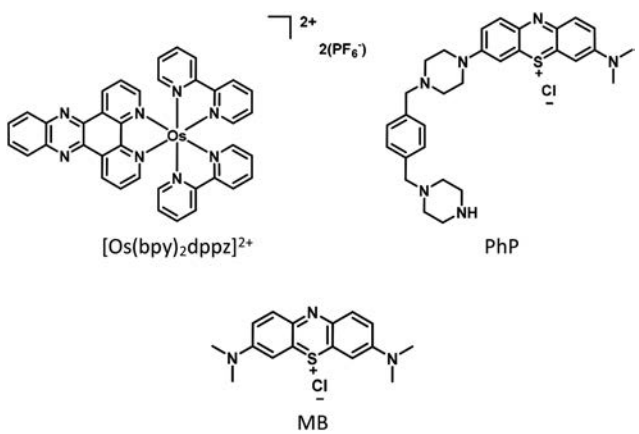

Fig. 1 Chemical structures of the 3 redox probes.

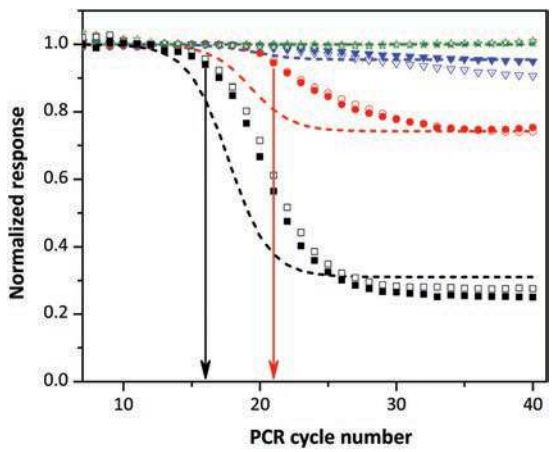

Fig. 2 Electrochemical qPCR curves (duplicates) of 10^7 target DNA copies of the LITMUS 28i vector in the presence of (open and filled black squares) 0.5 μM $[Os(bpy)_2dppz]^{2+}$, (open and filled red circles) 15 μM PhP, or (open and filled blue triangles) 15 μM MB. The two arrows indicate the cycle threshold for the $[Os(bpy)_2dppz]^{2+}$ and PhP probes, corresponding here to a 5% signal decrease. The horizontal plots (green stars) are negative controls (0 copies). Dashed lines are the predicted qPCR curves using eqn (7) (see the Experimental section) and the following set of parameters: K_b reported at 70 °C in Table 1, $N_i = 10^7$ copies, ε = 1.95, V = 50 μL, L = 150, $N_{max} = 3 \times 10^{12}$ copies, s = 2.5, Q_p^∞/Q_p^0 = 10 and C_I^0 = 15 μM for PhP and MB, and Q_p^∞/Q_p^0 = 200 and C_I^0 = 0.5 μM for $[Os(bpy)_2dppz]^{2+}$.

baseline background noise), was found to be 16.5 cycles for $[Os(bpy)_2dppz]^{2.+}$, 21 cycles for PhP and ~31 for MB (the last being difficult to extract accurately on account of the too small ~10% maximal amplitude signal decrease compared to the 30% and 70% with PhP and $[Os(bpy)_2dppz]^{2+}$, respectively).

To better understand and rationalize the marked differences observed among the three redox probes, the temperature dependence of K_b was evaluated. Toward this end, electrochemical binding titration experiments were performed at temperatures ranging from 20 to 70 °C using calf thymus as the ds-DNA titrant. These experiments were achieved using the same device as for electrochemical qPCR, taking advantage of the parallel heating and electrochemical addressing of multiple solutions (see the Experimental section for details). From the experimental titration curves obtained by plotting the normalised SWV peak charged as a function of ds-DNA concentration (Fig. S2–S7, ESI†) values of K_b were extracted from the best fitting of eqn (2) (see the Experimental section) to the data. The K_b values determined for each redox probe at different temperatures are reported in Table 1 and presented in Fig. 3 as Van't Hoff plots. At 20 °C, K_b values are close to those previously reported at room temperature,[8,10–12] while upon increasing the temperature they were all observed to decrease, a behaviour characteristic of a favourable exothermic binding reaction. The good linearity of the Van't Hoff plots indicates a constant standard enthalpy and entropy changes over the temperature. Thus the slopes of these linear plots allow for a direct side-by-side comparison of probes, whose enthalpy and entropy contributions are clearly not the same. Albeit the PhP molecule has the drawback at 20 °C of having 4-fold less affinity for ds-DNA than $[Os(bpy)_2dppz]^{2+}$, it is interesting to note that, on account of its smaller K_b temperature dependence, it reaches a two times lower affinity than the osmium probe at ~70 °C. Such a PhP behaviour is clearly useful for maintaining the probe affinity binding to ds-DNA as high as possible under the qPCR measurement conditions. In the case of MB, the combined effects of pronounced temperature dependence of K_b with an intrinsic low affinity binding reveals a very low value of K_b at ~70 °C (Table 1), a result that is finally consistent with the poor efficiency of MB in real-time electrochemical PCR.

Table 1 Binding constant (K_b in M^{-1}) of the redox probes for calf-thymus ds-DNA as a function of temperature. The binding site sizes were 2.8, 2.3 and 2.5 base pairs for $[Os(bpy)_2dppz]^{2+}$, PhP and MB, respectively

	K_b ($\times 10^5$ M^{-1})		
Temperature (°C)	$[Os(bpy)_2dppz]^{2+}$	PhP	MB
20	17.0 ± 4.8	4.2 ± 0.9	0.70 ± 0.20
30	12.0 ± 3.0	3.5 ± 0.8	0.50 ± 0.10
40	8.0 ± 2.0	3.0 ± 0.7	0.30 ± 0.06
50	5.5 ± 1.2	2.5 ± 0.5	0.21 ± 0.04
60	4.0 ± 0.8	1.7 ± 0.3	0.14 ± 0.03
70	3.0 ± 0.7	1.4 ± 0.2	0.08 ± 0.02

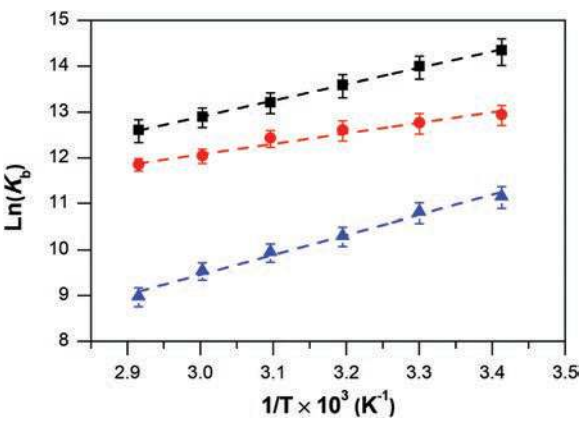

Fig. 3 Van't Hoff plots of $[Os(bpy)_2dppz]^{2+}$ (black squares), PhP (red circles) and MB (blue triangles). Dashed lines are the linear fits to the data.

To understand the temperature dependence of K_b obtained in Fig. 3, the molecular interactions between the different redox probes and ds-DNA were investigated with the help of molecular dynamic (MD) simulations. The computational protocol (see the Experimental section) is the same as the one we have recently used to evaluate the interaction energies between different osmium bipyridyl complexes and ds-DNA.[14] MD simulations (Fig. S8–S16, ESI†) show that for $[Os(bpy)_2dppz]^{2+}$ and MB, the intercalation binding modes arising from π–π interactions are more stable than others, while for PhP minor groove binding can also lead to a stable adduct, thanks to the formation of H bonds between the probe and ds-DNA. When the temperature increases, the intercalation binding modes are strongly affected by the structural distortion of the intercalation pocket, leading to a lessening of π–π interactions and a strong decrease of the affinity between the probe and ds-DNA. Contrary to the former probes, with PhP, the minor groove binding is characterised by a high flexibility that allows for the preservation of H bond interactions and softens the temperature dependant behaviour of the probe/DNA affinity as shown in the experiments of Fig. 3.

Taking into account the equilibrium distribution of the intercalating redox probe between its free and bound forms using the determined values of K_b at ~70 °C, the limited extent of amplicon growth at the end of PCR (~100 nM amplicon, which is equivalent to $N_{max} = 3 \times 10^{12}$ ds-DNA copies in 50 μL, see the ESI†), and the exponential growth rate equation of PCR, one can calculate the theoretical electrochemical qPCR kinetic curves using eqn (7) reported in the Experimental section. As shown in Fig. 2, the calculated curves (dashed lines) fit qualitatively quite well with the experimental data, especially the maximal signal amplitude decrease, meaning that the theoretical model with its associated experimental parameters (notably N_{max} and K_b) remains valid under PCR conditions. The main divergence is regarding the positions of the onset signal decrease which, for the theoretical plots, are all offset at slightly lower PCR cycle numbers than the experimental ones. Different reasons may explain this discrepancy.

The first one is a likely inhibitory effect of the redox probes on the PCR reaction, leading to a delay in the exponential growth rate of the amplicon (see Fig. S17, ESI†). Another possible account, especially in the case of PhP and MB probes, is that the recorded signal decrease is no longer in the exponential amplification phase of PCR but rather in the linear phase. Apart from this issue, one can point out the rather excellent homothety between the theoretical plot of the osmium complex (black dashed curve in Fig. 2) and the experimental ones (black square symbols in Fig. 2), the latter finally showing a well-defined exponential phase over a large part of the signal decrease.

To highlight the key parameters that influence the C_T value and thus the analytical performances of the method, the theoretical equation used to calculate the electrochemical qPCR kinetic plots was rearranged with a view to express C_T as follows:

$$C_T = \frac{1}{\log \varepsilon}\left[\log\left(\frac{1}{K_b} + C_I^0\right) + \beta\right] \quad (1)$$

where ε is the PCR efficiency and β is a term depending on the initial amount of the targeted DNA (see the Experimental section). Whatever the value of β, this expression highlights the interplay between K_b and C_I^0, as well as its influence on C_T. It notably shows that for reaching an optimal value of C_T (*i.e.*, a low C_T value in order to maximize the qPCR detection sensitivity), it is necessary to adjust the concentration C_I^0 at a value lower than $1/K_b$. Under these conditions, eqn (1) simplifies into $C_T = (\log \varepsilon)^{-1}[\log(1/K_b) + \beta]$, demonstrating then that for further decreasing C_T, it is necessary to improve K_b through the finding of a stronger affinity binding redox probe. To better illustrate this, a graphical 3D representation of the theoretical variations of C_T with K_b and C_I^0 at a fixed initial amount of the 10^7 copies of the DNA target is shown in Fig. 4. The three investigated probes are also reported on the graph, taking into account their theoretical C_T value at 10^7 copies (extracted from Fig. 2), their corresponding concentration in PCR experiments, and their ds-DNA binding constant at 70 °C (Table 1). For both the $[Os(bpy)_2dppz]^{2+}$ and MB probes, no significant improvement of C_T can be expected by lowering C_I^0 (see arrows 1 and 2 in Fig. 4). This is because the experimental concentration of C_I^0 has been chosen to be smaller than $1/K_b$. The only way to further improve the PCR sensitivity is to chemically modify the $[Os(bpy)_2dppz]^{2+}$ and MB probes by suitable functional groups with a view to increase their K_b values (arrows 3 to 4). This is typically what has been done through the chemical modification of MB into PhP (arrow 4). A closer examination of the PhP data reported in Fig. 4 shows that the probe concentration selected for the experiments is almost equal to $1/K_b$. This information tells us that the qPCR sensitivity could be somewhat optimized by decreasing C_I^0 (arrow 5).

As the $[Os(bpy)_2dppz]^{2+}$ leads to the lowest C_T values and largest signal amplitude decreases, including a well-defined exponential amplification phase, it has been next used to assess the analytical performances of our electrochemical qPCR system. Duplicate electrochemical qPCR amplifications were performed from 10-fold serial dilutions of a LITMUS 28i vector standard solution to obtain a range of initial target ds-DNA ranging from 10^8 to 10 copies per electrochemical microwell. Fig. 5 shows the resulting processed electrochemical qPCR kinetic curves (raw and baseline corrected data are

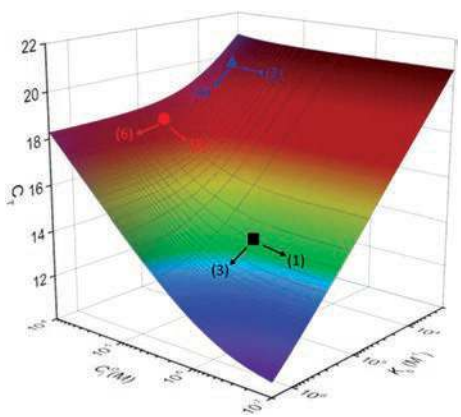

Fig. 4 Semi-logarithmic 3D plot of C_T as a function of C_I^0 and K_b. The C_T was calculated with eqn (1) and using the following parameters: α = 0.04, N_i = 10^7 DNA copies, V = 50 µL, L = 150 bp, s = 2.5 bp, and ε = 1.95. The black square, red circle and blue triangle symbols correspond to the $[Os(bpy)_2dppz]^{2+}$, PhP and MB probes, respectively (see the text for signification of the arrows).

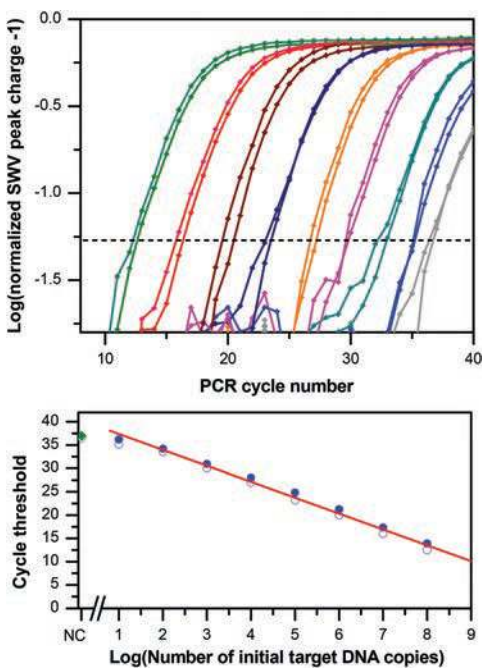

Fig. 5 Top: electrochemical qPCR amplification curves obtained in the presence of 0.5 µM $[Os(bpy)_2dppz]^{2+}$ and (green) 10^8, (red) 10^7, (brown) 10^6, (dark blue) 10^5, (orange) 10^4, (pink) 10^3, (cyan) 10^2, (blue) 10, and (grey) 0 target DNA copies of the LITMUS 28i vector per well (in duplicates). The horizontal dashed line is the threshold defined as 4 times the baseline noise. Bottom: calibration plot of C_T as a function of the initial target DNA content. The red line is the linear fit to the experimental data (ε = 1.96 and R^2 = 0.997) and the green diamond symbols are the negative controls (NC, no target DNA).

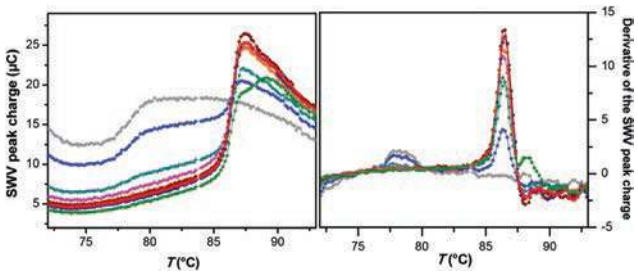

Fig. 6 Melting curve analysis performed immediately after the electrochemical qPCR amplifications shown in Fig. 5. Left: Raw melting curves resulting from the plot of the $[Os(bpy)_2dppz]^{2+}$ SWV peak charge as a function of linear ramp of temperature applied to the samples (ramp of 1 °C min^{-1} ranging from 60 °C to 95 °C). The colour code is the same as in Fig. 5: (green) 10^8, (red) 10^7, (brown) 10^6, (dark blue) 10^5, (orange) 10^4, (pink) 10^3, (cyan) 10^2, (blue) 10 and (grey) 0 copies of the LITMUS 28i vector per microwell. Right: First order derivative of the melting curves shown on the left graph. All first order derivative melting curves of positive samples (ranging from 10^8 to 10 copies) give a maximum peak at an average melting temperature of 86.4 ± 0.2 °C, characteristic of the right amplified amplicon, while for the 0 copy (negative control), a maximum peak localised at a melting temperature of ~78 °C suggests the presence of the short ds-DNA sequence, characteristic of non-specifically amplified primer dimers.

shown in Fig. S18, ESI†) as well as the extracted calibration plot. The linear relationship observed between C_T and the semi-log of initial DNA copies is in full agreement with the exponential reaction kinetics of PCR during its initial phase, finally leading to a PCR efficiency close to the theoretical value of 2. The linearity over 7 orders of magnitude also highlights the remarkable dynamic range (from 10 to 10^8 copies) of the method, offering the possibility to reach a detection limit as low as a few DNA copies per well. Moreover, the small standard deviations (on average ± 0.4 C_T) recovered from duplicated measurements attest of a rather good reproducibility. The non-specific signal decreases recorded for the negative controls (no DNA target) after more than 36 PCR cycles are the result of nonspecific amplification of primer dimers. This has been confirmed from the electrochemical melt curve analysis performed immediately after the PCR amplification (Fig. 6), showing a small transition at a temperature much lower than the amplicon.

Conclusions

To the best of our knowledge, the analytical performances of the current electrochemical qPCR outperform all those previously published.[6–9] In terms of detection limit, dynamic range, reproducibility and melting curve analysis, the current results are comparable with those obtained on a bench-top fluorescence-based qPCR instrument (compare Fig. 5 and 6 to Fig. S19 and S20, ESI†). This is an important result if one wishes to consider the commercial development of this new type of qPCR in the near future. In addition, the present electrochemical qPCR device has the merit to offer a decisive advantage over commercially available fluorescence-based qPCR instruments, that is, a much lower instrumental cost for similar performances and capabilities, including a smaller footprint and size. The prototype we have here developed is indeed built around a simple standard PCR thermocycler and the additional costs related to the dedicated multiplexed electronic board as well as to the specific disposable electrochemical microplates (a little more expensive to mass-produce than the standard PCR microplates) are negligible. This means that for an investment cost roughly similar to that of a standard PCR thermocycler, one can get the benefits of a qPCR instrument (in the case of fluorescence-based qPCR, the additional cost is at least two to three times higher than for a standard PCR thermocycler).

In conclusion, the results we have obtained in the current work definitely demonstrate the potentialities offered by the electrochemical qPCR method, which on account of the numerous advantages, holds great promise for the development of less expensive, more robust, smaller size and portable qPCR devices.

Experimental

Chemicals and reagents

All chemicals were of analytical grade and were used without further purification (excepted calf-thymus DNA). All reagents were purchased from Sigma-Aldrich unless otherwise stated. The osmium complex $[Os(bpy)_2dppz](PF_6)_2$ (where bpy = 2,2′-bipyridine and dppz = dipyrido[3,2-*a*:2′,3′-*c*]phenazine) and the methylene blue derivative PhP (7-dimethylamino-3-(1,10-[1,4-phenylenebis-(methylene)bispiperazine])-phenothiazin-5-ium chloride) were synthesised according to published procedures.[15,16] EvaGreen® was used as the fluorescent dye in the real time PCR experiment. All solutions were prepared using molecular biology grade water (DNAase, RNAase and protease free, Life Technologies). LITMUS 28i, a plasmid vector from *E. coli* ER2738, was purchased from New England Biolabs Inc. The reagents used in PCR reactions were purchased from Qiagen®: 10× PCR buffer (proprietary commercial buffer with Tris-Cl, KCl, $(NH_4)_2SO_4$ and 1.5 mM of $MgCl_2$, pH 8.7 at 20 °C), 10 mM dNTPs, and 5 U μL^{-1} HotStarTaq® DNA polymerase. Primers were designed using Primer3 (v. 0.4.0) (http://frodo.wi.mit.edu/primer3/), synthesised by Eurogentec and prepared as 100 μM stock solutions in water. The primer sequences used in this study are for the forward primer (lit28iFP-150): 5′-CCC GAG ATA GGG TTG AGT GTT GT-3′ and for the reverse primer (lit28iRP-150): 5′-CCT CGA CCC CAA AAA ACT TGA-3′. This set of primers allows the amplification of a 150 bp sequence at the position 1216–1366 in the LITMUS 28i vector sequence.

Electrochemical qPCR experiments

Electrochemical qPCR experiments were performed in 1× Qiagen PCR buffer containing 0.025 wt% bovine serum albumin (BSA), 1 wt% polyvinylpyrrolidone (PVP, MW 40 kDa),

Scheme 1 (A) Overview of the real-time electrochemical qPCR prototype that monitors, in parallel, up to 48 PCR reactions. (B) Flat Peltier-heating block and its two 72-pin connectors mounted in a standard PCR thermocycler. (C) Disposable 48-well electrochemical microplate (the inset shows a zoom on the electrochemical microwells equipped at their flat bottom with three screen-printed electrodes).

200 μM of each dNTP, 1.25 U HotStarTaq Plus DNA polymerase (0.025 U μL^{-1}), 200 nM of each primer, different amounts of the LITMUS 28i vector template (10 to 10^8 copies per PCR mixture) and either 0.5 μM $[Os(bpy)_2dppz]^{2+}$, 10 μM PhP or 10 μM MB.

Real-time electrochemical monitoring of PCR reactions was run in an automated house-build prototype instrument (Scheme 1)[13] (co-developed with the Easy Life Science company) consisting of a disposable electrochemical microplate of 48 flat-bottom electrochemical wells fastened over a flat Peltier-heating block and wired electrically to a PCB interface containing the electronic circuitry of the multiplexed potentiostat. Each well of the microplate, integrating three screen-printed electrodes, was filled with 50 μL of the PCR reaction mixture and sealed with an optical adhesive film (MicroAmp, Thermo Fisher Scientific).

The PCR reactions were run at 93 °C for 15 min, followed by 50 cycles at 93 °C for 90 s, 60 °C for 150 s, and 72 °C for 30 s. The content of each of the 48-electrochemical wells was scanned by square wave voltammetry (SWV) at the end of the elongation step (*i.e.*, at 72 °C) of each PCR cycle (at a maximal sampling rate of 0.3 Hz). The SWV parameters were 50 Hz frequency, 40 mV half-wave amplitude and 1 mV potential step, while the scanned potential windows were from 400 to 900 mV for $[Os(bpy)_2dppz]^{2+}$, 25 to −475 mV for MB and 150 to −350 mV for PhP (*vs.* a pseudo silver reference electrode). The SWV peak current was automatically baseline-corrected and integrated from each scan, and the peak charge reported as a function of the PCR cycle number. The resulting amplification curves were corrected from the signal drift observed in the absence of the specific signal decrease by subtracting a least-squares fitted line across the first cycles and then offsetting the data sets to align the value of these corrected cycles.

Melt curve analysis was run immediately after the PCR amplification, starting with a denaturation step at 93 °C for 90 s followed then by a cooling step at 50 °C for 5 min, and next a 1 °C min^{-1} linear ramp of temperature (from 60 °C to 92 °C) during which SWV scans were recorded every 0.5 °C (using the same SWV parameters as during the PCR). The resulting SWV peak charges were reported as a function of the temperature.

DNA quantification at end-point PCR was carried out with a Qubit™ Fluorometer® using the Qubit™ dsDNA HS Assay Kits, following the manufacturer's (Thermo Fisher) recommendations. The end-point DNA concentration was found to be ~1.6×10^{-7} M, ~0.8×10^{-7} M, and ~0.8×10^{-7} M for PCR experiments involving $[Os(bpy)_2dppz]^{2+}$, PhP and MB, respectively (an average value of 1.07×10^{-7} M was used for the calculation of theoretical qPCR plots in Fig. 2).

Fluorescence qPCR experiments

Real-time fluorescence monitoring of DNA amplification was performed in the presence of EvaGreen® using a 7500 ABI Fast Real-Time PCR machine (Applied Biosystem Instruments). All fluorescence PCR mixtures (20 μL) consisted of the same components as for electrochemical qPCR except that the redox probe was replaced with a 1× EvaGreen® fluorescent probe. Real-time monitoring of DNA amplification was performed at 95 °C for 15 min, followed by 50 cycles at 95 °C for 60 s and 60 °C for 120 s. The fluorescence signal was measured at the end of each PCR cycle (*i.e.*, at 60 °C).

Melt curve analysis was run immediately after the PCR amplification, starting with a denaturation step at 95 °C for 10 s followed then by a cooling step at 60 °C for 60 s, and next a 1 °C min^{-1} linear ramp of temperature (from 60 °C to 95 °C) during which the fluorescence signal was recorded at every 0.5 °C. Raw fluorescence data were collected and treated in real-time using 7500 software v2.0.5 from Thermo Fisher Scientific.

Electrochemical determination of K_b as a function of temperature

All binding constant measurements were performed in 5 mM Tris buffer (pH 8.3, 25 °C) containing 55 mM KCl and 1 wt%. PVP. The redox probes were added in the buffer solution at a final concentration of 20 μM and titrated by calf thymus double-strand DNA (type I, highly polymerised). The latter was desalted beforehand using an Amicon 30 kDa molecular weight cut-off centrifugal filter (Merck Millipore) and quantified using a Nanodrop2000 spectrometer (Thermo Scientific) using $\varepsilon_{260} = 6600\ M^{-1}\ cm^{-1}$.

The electrochemical measurements of the binding constant were performed with the same house-built automated electrochemical readout device as the one used for our electrochemical qPCR experiments. For each experiment, an electrochemical microplate was filled with 40 μL of buffer solutions containing 20 μM of the redox probe. After the electrochemical wells were sealed with an optical adhesive film, a thermal cycle consisting of a staircase ramp of temperatures was then applied to the overall solutions, starting first by a temperature step of 8 min at 20 °C followed by a series of temperature steps of 4 min at 30, 40, 50, 60 and 70 °C (Fig. S2–S4, ESI†), before

turning back to the initial temperature of 20 °C. During the thermal cycle, the overall solutions were scanned by SWV every 40 s (the SWV parameters and scanned potential windows were the same as for the electrochemical qPCR experiments). Then, after removing the adhesive film, 2 μL of different standard calf-thymus ds-DNA solutions were injected into the electrochemical wells in such a way as to obtain a suitable range of ds-DNA concentrations distributed over the microplate. Then, after sealing the wells again with an adhesive film, a second thermal cycle, identical to the first one, was applied to the overall mixtures and the SWV responses were recorded as previously (Fig. S2–S4, ESI†). For each scan, the current peak was automatically baseline corrected and integrated. The normalised peak charge was obtained from the ratio between the peak charge (Q_p) recorded at equilibrium for a given temperature and the ds-DNA concentration, and the initial peak charge (Q_p^0) recorded at the same temperature but before the addition of ds-DNA. The normalised peak charge (Q_p/Q_p^0) was determined for each temperature step and the DNA concentration was averaged over 3 SWV scans performed over 3 replicated experiments, before then being plotted as a function of the ds-DNA concentration for each temperature (Fig. S5–S7, ESI†). The resulting titration plots were then fitted with the theoretical eqn (2) which assumes a classical law of mass action between the intercalating species and the binding sites of ds-DNA (including a predetermined number of non-cooperative binding sites per unit of ds-DNA) and fast equilibrium binding reached at any time during the titration experiment:[17]

$$\frac{Q_p}{Q_p^0} = 1 - \frac{\frac{1}{K_b} + C_I^0 + \frac{C_{DNA}^0}{s} - \sqrt{\left(\frac{1}{K_b} + C_I^0 + \frac{C_{DNA}^0}{s}\right)^2 - 4C_I^0\frac{C_{DNA}^0}{s}}}{2C_I^0} \times \left(1 - \frac{Q_p^\infty}{Q_p^0}\right) \quad (2)$$

where Q_p^∞ is the peak charge at an extrapolated infinite concentration of ds-DNA, K_b is the binding constant, C_I^0 is the total intercalating probe concentration, C_{DNA}^0 is the total concentration of the DNA base pair and s is the binding site size (number of base pairs involved in a binding site). From the best fits of eqn (2) to the experimental data, the parameters K_b, s and Q_p/Q_p^∞ were determined. The binding site size s was found between 2 and 3 base pairs, depending on the intercalating probe, a value which is in the same range to that previously reported with small DNA intercalating probes.[8,15,18]

Establishment of the theoretical equations used to predict the kinetic qPCR curves

The combination of eqn (2) with the basic exponential growth rate equation of PCR, *i.e.* $N_C = N_i\varepsilon^C$ (where N_C is the copies number of the amplified ds-DNA amplicon after C cycles, N_i is the initial copy number of the DNA target, and ε is the amplification efficiency) leads to a general expression allowing us to calculate the normalised peak charge decrease as a function of PCR cycles. For such a purpose, C_{DNA}^0/s (*i.e.*, the total concentration of ds-DNA intercalating binding sites) in eqn (2) has to be replaced by the following expression:

$$\frac{C_{DNA}^0}{s} = \frac{L}{sVN_A}N_i\varepsilon^C \quad (3)$$

where L is the length of the amplified DNA sequence, N_A is the Avogadro constant and V is the volume of the PCR solution. The general expression is thus finally given by eqn (4).

$$\frac{Q_p}{Q_p^0} = 1 - \frac{\frac{1}{K_b} + C_I^0 + \frac{L}{sVN_A}N_i\varepsilon^C - \sqrt{\Delta}}{2C_I^0} \left(1 - \frac{Q_p^\infty}{Q_p^0}\right) \quad (4)$$

$$\text{with } \Delta = \left(\frac{1}{K_b} + C_I^0 + \frac{L}{sVN_A}N_i\varepsilon^C\right)^2 - 4C_I^0\frac{L}{sVN_A}N_i\varepsilon^C$$

To consider the limited extent of amplicon growth in PCR, reaching a saturating value, the classical exponential growth rate equation of PCR can be replaced by the following limited exponential growth rate equation:

$$N_C = \frac{N_{max}}{1 + \frac{N_{max}}{N_i}\varepsilon^{-C}} \quad (5)$$

where N_{max} is the maximal number of copies of ds-DNA that can be produced at the end of PCR. At a low amount of amplified DNA (*i.e.*, $N_{max}\varepsilon^{-C}/N_i \gg 1$), eqn (5) reduces to the standard exponential law of PCR (*i.e.* $N_C = N_i\varepsilon^C$), while at a low value of N_{max} and high values of N_i and/or C (*i.e.*, when $N_{max}\varepsilon^{-C}/N_i \ll 1$), eqn (5) becomes equal to N_{max} (*i.e.*, the maximal amount of the DNA amplicon that can be produced).

Conversion of eqn (5) into the concentration of ds-DNA intercalating binding sites leads to:

$$\frac{C_{DNA}^0}{s} = \frac{L}{sVN_A}\frac{N_{max}}{\left(1 + \frac{N_{max}}{N_i}\varepsilon^{-C}\right)} \quad (6)$$

which once incorporated into eqn (4) leads to eqn (7) which can then be used to simulate normalised real-time PCR curves (valid for either normalised peak currents or peak charges).

$$\frac{Q_p}{Q_p^0} = 1 - \frac{\frac{1}{K_b} + C_I^0 + \frac{L}{sVN_A}\frac{N_{max}}{1 + \frac{N_{max}}{N_i}\varepsilon^{-C}} - \sqrt{\Delta}}{2C_I^0} \left(1 - \frac{Q_p^\infty}{Q_p^0}\right) \quad (7)$$

$$\text{with } \Delta = \left(\frac{1}{K_b} + C_I^0 + \frac{L}{sVN_A}\frac{N_{max}}{1 + \frac{N_{max}}{N_i}\varepsilon^{-C}}\right)^2 - 4C_I^0\frac{L}{sVN_A}\frac{N_{max}}{1 + \frac{N_{max}}{N_i}\varepsilon^{-C}}$$

Demonstration of eqn (1)

Eqn (2) is rearranged to include Q_p^∞ in the normalised peak charge and to eliminate the denominator on the right part, leading then to eqn (8):

$$\frac{Q_p^0 - Q_p}{Q_p^0 - Q_p^\infty} = \frac{1}{2}\left(1 + \frac{1}{K_b C_I^0} + \frac{C_{DNA}^0}{sC_I^0} - \sqrt{\left(1 + \frac{1}{K_b C_I^0} + \frac{C_{DNA}^0}{sC_I^0}\right)^2 - 4\frac{C_{DNA}^0}{sC_I^0}}\right) \quad (8)$$

When the amplification reaches the C_T, the base pair concentration at the cycle threshold $C_{DNA}^{C_T}$ can be obtained from the basic exponential growth rate equation of PCR:

$$C_{DNA}^{C_T} = C_{DNA}^0 = C_{DNA}^i L \varepsilon^{C_T} \quad (9)$$

with C_{DNA}^i as the initial concentration of the DNA target (in M of copies).

If one wants to take into account the limited production of the amplicon at the end of PCR, eqn (9) has to be replaced by eqn (10):

$$C_{DNA}^{C_T} = C_{DNA}^0 = \frac{LC_{DNA}^{max}}{1 + \frac{C_{DNA}^{max}}{C_{DNA}^i}\varepsilon^{-C_T}} \quad (10)$$

where C_{DNA}^{max} is the maximal concentration of the ds-DNA amplicon that can be produced at the end of the PCR amplification.

We define α as the normalised peak charge threshold value, *i.e.* the value of the onset peak charge decrease corresponding to the C_T value. The value of α is generally adjusted by the experimenter in such a way to have a significant signal/noise ratio. It can thus be defined, for instance, as being 4-fold the standard deviation of the normalized background response determined during the first PCR cycles (*i.e.*, when the signal remains stable). Typical α values in the range of 0.03 to 0.05 were used. Thus, at the cycle threshold, eqn (8) can be written as:

$$\alpha = \frac{1}{2}\left(1 + \frac{1}{K_b C_I^0} + \frac{C_{DNA}^{C_T}}{sC_I^0} - \sqrt{\left(1 + \frac{1}{K_b C_I^0} + \frac{C_{DNA}^{C_T}}{sC_I^0}\right)^2 - 4\frac{C_{DNA}^{C_T}}{sC_I^0}}\right) \quad (11)$$

Eqn (9) was then rearranged to express $C_{DNA}^{C_T}$ as a function of overall parameters, leading to eqn (12):

$$C_{DNA}^{C_T} = s\frac{\alpha}{1-\alpha}\left[\frac{1}{K_b} + C_I^0(1-\alpha)\right] \quad (12)$$

In order to express the parameter C_T as a function of ε, C_{DNA}^i, K_b, and C_I^0, $C_{DNA}^{C_T}$ has to be replaced by eqn (9) or (10), thus leading after rearrangement to eqn (13) or (14), respectively:

$$C_T = \frac{1}{\log \varepsilon}\left\{\log\left[\frac{1}{K_b} + C_I^0(1-\alpha)\right] + \log\left[\frac{s}{C_{DNA}^i L}\left(\frac{\alpha}{1-\alpha}\right)\right]\right\} \quad (13)$$

$$C_T = \frac{1}{\log \varepsilon}\left\{\begin{array}{l}\log\left[\frac{1}{K_b} + C_I^0(1-\alpha)\right] \\ -\log\left[\frac{C_{DNA}^i L}{s}\left(\frac{1-\alpha}{\alpha}\right) - \frac{C_{DNA}^i}{C_{DNA}^{max}}\left(\frac{1}{K_b} + C_I^0 - C_I^0\alpha\right)\right]\end{array}\right\} \quad (14)$$

As $\alpha \ll 1$ and assuming in eqn (14) that:

$$\frac{1}{C_{DNA}^{max}}\left(\frac{1}{K_b} + C_I^0 - C_I^0\alpha\right) \ll \left(\frac{1-\alpha}{\alpha}\right)\frac{L}{s}$$

(which is true if C_{DNA}^{max} and K_b are high and/or C_I^0 is low, meaning also that the maximal signal amplitude decrease is much larger than the signal decrease threshold), then both eqn (13) and (14) can be approximated by the same eqn (15):

$$C_T = \frac{1}{\log \varepsilon}\left\{\log\left[\frac{1}{K_b} + C_I^0\right] + \log\left(\frac{\alpha s}{C_{DNA}^i L}\right)\right\} \quad (15)$$

This equation is equivalent to eqn (1) in which $\beta = \log(\alpha s/C_{DNA}^i L)$ is a term independent of K_b and C_I^0 and is a function of the starting amount of the target DNA.

Molecular dynamics study of DNA–probe complexes

To evaluate the affinity between the probes and a double-strand DNA, we relied on a computational protocol based on a molecular dynamics (MD) simulation of the DNA–probe complex that we have recently developed.[13]

The MD simulations of the DNA–probe complexes were performed by using the GROMACS.v.5.0.5 package.[19] The initial structure of the B-DNA dodecamer (Drew–Dickerson dodecamer)[20] with 12 base pairs (bp) d(CGCGAATTCGCG)$_2$ was obtained from the Nucleic Acid Database[21] with the PDB code 1BNA. The ff99 set of parameters with the PARMBSC0 modification was employed for the nucleic acid 1BNA. GAFF parameters[22] were used for the three probes as well as the parameters we recently developed for the Os(II) metallointercalators to describe Os–N bonds, Os–N–C and N–Os–N angles and all torsion angles involving Os(II).

For each probe, we generated different initial DNA-complexes in which the probe was manually placed in different binding sites of the DNA. For $[Os(bpy)_2dppz]^{2+}$, we have considered one binding site, namely intercalation in the major groove (Int-Major) (Fig. S8†). In our previous work,[13] we have indeed demonstrated that this intercalation binding mode is more stable than others (intercalation in the minor groove, minor groove binding, major groove binding and external to the phosphates). For this intercalation binding mode, the dppz group of $[Os(bpy)_2dppz]^{2+}$ was inserted into the major groove $(AATT)_2$ of the 1BNA between the base pair steps 5′-A_5-A_6-3′ and 5′-T_{19}-T_{20}-3′, respectively, with the cyclic ring system of the probes being perpendicular to the helical axis.

For MB and PhP, we have considered three different binding modes: symmetric intercalation, perpendicular intercalation and minor groove binding (Fig. S9†). As a matter of fact, in a recent publication dedicated to the binding modes of MB and DNA, Nogueira and González[23] have compared the external, intercalative, minor groove, and major groove

binding modes with the help of energetic and structural analyses. They have found out that minor groove and intercalative binding leads to stable adducts.

The whole system was inserted into a cubic box of 1.5 nm around the DNA–probe complex using periodic boundary conditions. The system was solvated with 13 376–13 403 water molecules using the TIP3P/SPC water model.[24] For Os(II) probes, the total charge of the DNA–probe complex system was −20 which was neutralized by adding 20 Na^+ counterions. For MB and PhP, the total charge is −21 and 21 Na^+ counterions were added.

For the three probes, additional 26 Na^+ and Cl^- ions were included to set the solution ionic strength to about 100 mM. In the first stage of MD simulation, the DNA–probe complex was fixed, and water and ion positions were minimised using the steepest descent method for 1000 steps. Then, the minimised system was slowly heated to 25 °C for 100 ps (time steps = 0.002 and *n* steps 50 000) with the leap-frog integrator *via* the NVT ensemble. During the dynamics, the temperature was maintained constant at 25 °C or 70 °C with the help of the Berendsen thermostat.[25] A canonical ensemble (NVT) was followed by isothermal–isobaric (NPT) ensemble for 100 ps, where the density of the system was equilibrated. The pressure coupling of 1 bar was provided with the Parrinello–Rahman method.[26] The Coulomb part was evaluated by means of the particle mesh Ewald (PME) method with a grid spacing of 1 Å in each direction. After the NPT ensemble, the final production molecular dynamics was performed for 10 ns and snapshots of the production simulations were recorded every 5 ps.

Acknowledgements

This work was supported by the LabEx MiChem (ANR-11-IDEX-0004-02) and a granted access to the HPC resources of CINES and IDRIS (2017-A0010810135) made by GENCI and MesoPSL (Equip@Meso, ANR-10-EQPX-29-01). The authors thank Prof. Kathryn B. Grant from Georgia State University for providing us the PhP molecule.

References

1 (*a*) A. Niemz, T. M. Ferguson and D. S. Boyle, *Trends Biotechnol.*, 2011, **29**, 240–250; (*b*) A. St John and C. P. Price, *Clin. Biochem. Rev.*, 2014, **35**, 155–167.
2 J. Wilhelm and A. Pingoud, *ChemBioChem*, 2003, **4**, 1120–1128.
3 G. J. Nixon, H. F. Svenstrup, C. E. Donald, C. Carder, J. M. Stephenson, S. Morris-Jones, J. F. Huggett and C. A. Foy, *Biomol. Detect. Quantif.*, 2014, **2**, 4–10.
4 D. Lee, P.-J. Chen and G.-B. Lee, *Biosens. Bioelectron.*, 2010, **25**, 1820–1824.
5 C. Lui, N. C. Cady and C. A. Batt, *Sensors*, 2009, **9**, 3713–3744.
6 S. S. W. Yeung, T. M. H. Lee and I. M. Hsing, *J. Am. Chem. Soc.*, 2006, **128**, 13374–13375.
7 T. Deféver, M. Druet, M. Rochelet-Dequaire, M. Joannes, C. Grossiord, B. Limoges and D. Marchal, *J. Am. Chem. Soc.*, 2009, **131**, 11433–11441.
8 T. Deféver, M. Druet, D. Evrard, D. Marchal and B. Limoges, *Anal. Chem.*, 2011, **83**, 1815–1821.
9 C. Toumazou, L. M. Shepherd, S. C. Reed, G. I. Chen, A. Patel, D. M. Garner, C.-J. A. Wang, C.-P. Ou, K. Amin-Desai, P. Athanasiou, H. Bai, I. M. Q. Brizido, B. Caldwell, D. Coomber-Alford, P. Georgiou, K. S. Jordan, J. C. Joyce, M. La Mura, D. Morley, S. Sathyavruthan, S. Temelso, R. E. Thomas and L. Zhang, *Nat. Methods*, 2013, **10**, 641–646.
10 T. W. Welch and H. H. Thorp, *J. Phys. Chem.*, 1996, **100**, 13829–13836.
11 L. Z. Zhang and G.-Q. Tang, *J. Photochem. Photobiol., B*, 2004, **74**, 119–125.
12 B. Wilson, M.-J. Fernandez, A. Lorente and K. B. Grant, *Tetrahedron*, 2008, **64**, 3429–3436.
13 (*a*) F. Kivlehan, F. Mavré, L. Talini, B. Limoges and D. Marchal, *Analyst*, 2011, **136**, 3635–3642; (*b*) A. Martin, L. Bouffier, K. B. Grant, B. Limoges and D. Marchal, *Analyst*, 2016, **141**, 4196–4203; (*c*) A. Martin, K. B. Grant, F. Stressmann, J.-M. Ghigo, D. Marchal and B. Limoges, *ACS Sens.*, 2016, **1**, 904–912.
14 A. Sharma, S. Delile, M. Jabri, C. Adamo, C. Fave, D. Marchal and A. Perrier, *Phys. Chem. Chem. Phys.*, 2016, **18**, 30029–30039.
15 B. Wilson, M.-J. Fernandez, A. Lorente and K. B. Grant, *Tetrahedron*, 2008, **64**, 3429–3436.
16 E. M. Kober, J. V. Caspar, B. P. Sullivan and T. J. Meyer, *Inorg. Chem.*, 1988, **27**, 4587–4598.
17 (*a*) M. T. Carter, M. Rodriguez and A. J. Bard, *J. Am. Chem. Soc.*, 1989, **111**, 8901–8911; (*b*) G. Scatchard, *Ann. N. Y. Acad. Sci.*, 1949, **51**, 660–672.
18 (*a*) M. Hossain, P. Giri and G. S. Kumar, *DNA Cell Biol.*, 2008, **27**, 81–90; (*b*) S. Nafisi, A. A. Saboury, N. Keramat, J.-F. Neault and H.-A. Tajmir-Riahi, *J. Mol. Struct.*, 2007, **827**, 35–43; (*c*) T. W. Welch, A. H. Corbett and H. H. Thorp, *J. Phys. Chem.*, 1995, **99**, 11757–11763.
19 D. Van der Spoel, E. Lindahl, B. Hess, G. Groenhof, A. E. Mark and H. J. C. Berendsen, *J. Comput. Chem.*, 2005, **26**, 1701–1718.
20 H. R. Drew, R. M. Wing, T. Takano, C. Broka, S. Tanaka, K. Itakura and R. E. Dickerson, *Proc. Natl. Acad. Sci. U. S. A.*, 1981, **78**, 2179–2183.
21 H. M. Berman, W. K. Olson, D. L. Beveridge, J. Westbrook, A. Gelbin, T. Demeny, S. H. Hsieh, A. R. Srinivasan and B. Schneider, *Biophys. J.*, 1992, **63**, 751–759.
22 J. M. Wang, R. M. Wolf, J. W. Caldwell, P. A. Kollman and D. A. Case, *J. Comput. Chem.*, 2004, **25**, 1157–1174.
23 J. J. Nogueira and L. González, *Biochemistry*, 2014, **53**, 2391–2412.
24 K. Toukan and A. Rahman, *Phys. Rev. B: Condens. Matter*, 1985, **31**, 2643–2648.
25 H. J. C. Berendsen, J. P. M. Postma, W. F. Vangunsteren, A. Dinola and J. R. Haak, *J. Chem. Phys.*, 1984, **81**, 3684–3690.
26 M. Parrinello and A. Rahman, *Phys. Rev. Lett.*, 1980, **45**, 1196–1199.